Journal of Alloys and Compounds 1040 (2025) 183625

Contents lists available at ScienceDirect

Journal of Alloys and Compounds

journal homepage: www.elsevier.com/locate/jalcom

Exploring p-type conductivity and homojunction devices in amorphous zinc tin nitride: A step toward enhanced nitride semiconductor applications

Nameun Kim [a,b,1], Ji Woon Choi [a,1], Wooseok Song [a,c], Saewon Kang [a], Soonmin Yim [a], Jung-Woo Yoo [b], Taek-Mo Chung [a,d,*], Ki-Seok An [a,d,*]

[a] Thin Film Materials Research Center, Korea Research Institute of Chemical Technology (KRICT), Daejeon 34114, Republic of Korea
[b] Materials Science & Engineering, Ulsan National Institute of Science & Technology (UNIST), 50, UNIST-gil, Eonyang-eup, Ulju-gun, Ulsan, Republic of Korea
[c] School of Electronic and Electrical Engineering, Sungkyunkwan University, Suwon, 16149, Republic of Korea
[d] Department of Chemical Convergence Materials, University of Science and Technology (UST), 217 Gajeong-ro, Yuseong-gu, Daejeon 34113, Republic of Korea

ARTICLE INFO

Keywords:
Ternary nitrides
Homojunctions
Amorphous materials
P-type semiconductors
PECVD

ABSTRACT

Nitride-based materials have garnered significant attention for next-generation optoelectronic devices owing to their tunable properties, which enable innovative device applications. Among these, zinc tin nitride (ZTN) is promising because of its unique electronic and optical characteristics. Herein, we report the first successful fabrication and characterization of p-n homojunction devices based on amorphous ZTN thin films doped with group III elements (Al and Ga). The doped ZTN thin films were synthesized using a modified pulsed plasma-enhanced chemical vapor deposition (PECVD) method, allowing precise control over the injection of each precursor for tailored material properties. Systematic doping of p-type ZTN with varying dopant concentrations revealed tunable optical and electrical properties, including hole concentrations ranging from 10^{13} to 10^{18} cm^{-3}, mobilities of ~1–10 $cm^2/(V{\cdot}s)$, bandgaps of 1.96–2.43 eV, work functions of 4.25–4.97 eV, and Fermi level modulation. The optimized ZTN-based homojunction device exhibited a rectification ratio of 10^2, which is attributed to band structure engineering of the p-type ZTN. This work highlights the potential of group III-doped ZTN as a scalable platform for high-performance optoelectronic devices and contributes to the advancement of nitride-based materials for next-generation devices.

1. Introduction

The development of nitride semiconductors is a critical challenge in advancing high-performance electronic and optoelectronic devices. Recent advances in nitride-based devices, such as AlN interlayer engineering for GaN heat dissipation [1], GaN avalanche photodetectors [2], and graphene/GaN ultraviolet detectors [3], highlight the increasing importance of nitride semiconductors in optoelectronic applications. Moreover, modern electronics increasingly require homojunction devices, in which both the p-type and n-type regions are formed from the same semiconductor material. This configuration enables efficient charge carrier transport across the junction, thereby enhancing overall device efficiency and reliability [4–7].

However, the tunability of electronic and optical properties in binary III-nitrides is inherently limited, restricting the range of achievable material characteristics. Recently, ternary nitrides—particularly II-IV nitrides such as zinc tin nitride (ZTN)—have emerged as attractive alternatives due to their compositional tunability, abundance, cost-effectiveness, low toxicity, and excellent optoelectronic properties, including a direct bandgap and high absorption coefficient [8–13]. In particular, ZTN is noteworthy because it exhibits defect-tolerant behavior, maintaining good optoelectronic performance even in the presence of structural imperfections. This property makes ZTN particularly promising for solar energy conversion applications, including photovoltaic (PV) and photoelectrochemical (PEC) devices [14]. In this context, ZTN offers a new pathway to overcome the intrinsic limitations of binary nitrides, while drawing insights from recent advances in nitride- and 2D material-based devices [1–3,15,16].

While high-quality n-type ZTN has been demonstrated, achieving stable and efficient p-type ZTN remains challenging due to difficulties in effective doping and maintaining stable hole concentrations. This is primarily attributed to intrinsic donor-type defects such as Sn_{Zn} anti-

* Corresponding authors at: Thin Film Materials Research Center, Korea Research Institute of Chemical Technology (KRICT), Daejeon 34114, Republic of Korea
E-mail addresses: tmchung@krict.re.kr (T.-M. Chung), ksan@krict.re.kr (K.-S. An).
[1] Nameun Kim and Ji Woon Choi contributed equally to this work

https://doi.org/10.1016/j.jallcom.2025.183625
Received 1 July 2025; Received in revised form 24 August 2025; Accepted 7 September 2025
Available online 9 September 2025

sites (Sn substituting Zn), V_N (N vacancies), and Zn_i (Zn in the interstitial site surrounded by N atoms), as well as extrinsic defects like O_N (O substituting N) [17–19]. Intrinsic donor defects have significantly lower formation energies than intrinsic acceptor defects, and thermodynamic analyses indicate that p-type doping of ZTN is highly challenging [17]. Nevertheless, Adamski et al. theoretically predicted p-type nitride semiconductors by doping Zn-IV nitrides with Li, Al, Ga, and In cations, while Chinnakutti et al. experimentally demonstrated the p-type conversion of ZTN through doping with Li and Ba via sputtering [20–22].

For enhanced p-type doping and effective suppression of donor defect formation, ZTN thin films should be synthesized as amorphous materials using chemical vapor deposition (CVD) [23]. Historically, ZTN thin films have typically been deposited by physical vapor deposition (PVD) techniques such as sputtering [21,22,24–28] or molecular beam epitaxy (MBE) [29,30], resulting in crystalline films—typically in wurtzite or orthorhombic phases. In such cases, ZTN exhibits high electron concentrations due to donor defects such as Sn_{Zn} and Zn_i. Compared to crystalline phases, amorphous ZTN lacks long-range periodicity and well-ordered atomic arrangements, which increases the formation energy of certain defects—such as donor-type interstitials or substitutional impurities—making their formation energetically unfavorable and thus more conducive to p-type conductivity [28]. However, synthesizing amorphous ZTN using conventional thermal CVD is difficult due to the low decomposition temperature of ZTN (~455 °C) [31] and the high temperatures required for activation of nitrogen precursors such as N_2 and NH_3 (600–800 °C) [32].

In this study, we report the synthesis of amorphous p-type ZTN thin films doped with Al and Ga using a modified pulsed plasma-enhanced chemical vapor deposition (PECVD) method, which enables low-temperature growth and precise dopant control through a sequential pulsing strategy. Unlike thermal CVD, PECVD utilizes plasma energy to drive chemical reactions, allowing deposition at much lower substrate temperatures and promoting amorphization by suppressing atomic diffusion and crystallization [33]. We examine the impact of dopant concentration on the chemical environment, electrical and optical properties, and band structure. Finally, we demonstrate the fabrication and characterization of p-n homojunction devices composed entirely of amorphous ZTN thin films, confirming their potential for next-generation optoelectronic applications.

2. Experiment

2.1. Deposition of nitride thin films

Al-doped ZTN (AZTN) and Ga-doped ZTN (GZTN) thin films were deposited on three different substrates—bare Si, dry-oxidized SiO_2 (100 nm)/Si, and soda-lime glass—using a custom-built pulsed PECVD system at a growth temperature of 300 °C. The bare Si substrate was used for analyses, such as XPS, EDS, and UPS, to accurately probe the intrinsic bonding environment of the thin films. The dry-oxidized SiO_2 (100 nm)/Si substrate was used to eliminate the electrical contribution from the Si during Hall-effect measurements and device characterizations. Lastly, the soda-lime glass substrate, being transparent and amorphous, was employed for XRD and UV-Vis analyses. All the substrates were cleaned sequentially with acetone, ethanol, and deionized water. Before each deposition, deposition chamber pretreatment was performed for 20 min by introducing remotely generated H_2 plasma to remove residual oxygen and moisture, thereby suppressing oxygen impurities in the nitride thin films. The H_2 plasma was generated by flowing ultrahigh-purity H_2 (99.9999 %) gas at a flow rate of 500 sccm with a plasma power of 50 W. AZTN thin films were prepared via the reaction of trimethyl aluminum (99.9999 %, $(CH_3)_3Al$, EG Chem Co., Ltd.), diethyl zinc (99.9999 %, $(C_2H_5)_2Zn$, EG Chem Co., Ltd.), tetrakis (dimethylamino) tin(IV) (99.9999 %, $[(CH_3)_2N]_4Sn$, EG Chem Co., Ltd.), and NH_3 (99.999 %) gas. Trimethyl aluminum (TMA) and diethyl zinc (DEZ) kept at 10 °C and tetrakis(dimethylamino) tin(IV) (TDMASn) heated to 50 °C were used as the Al, Zn, and Sn precursors, respectively. GZTN thin films were prepared similarly to the AZTN thin films using a novel Ga precursor, which was $C_5H_{13}OGa$ (99.35 %, Lake Materials Co., Ltd.). Flows of 99.999 % pure N_2 and NH_3 gases were used as the precursor delivery and nitrogen sources, respectively. Plasma was generated at 10 W to supply activated nitrogen. The flow rates of N_2 and NH_3 were adjusted to 10 and 200 sccm, respectively, using mass flow controllers.

2.2. Fabrication of devices

A custom thermal evaporator was utilized to fabricate the p-n homojunction devices. The bottom electrodes were deposited via thermal evaporation of Cr/Au (5/100 nm) on a dry-oxidized SiO_2 (100 nm)/Si substrate. Subsequently, n-type ZTN and p-type AZTN or GZTN thin films were deposited *in situ* on the bottom electrodes. Top electrodes of Cr/Au (5/100 nm) were deposited on the nitride thin films using a shadow mask. The top electrodes had diameters of 200 μm and were spaced 200 μm apart.

2.3. Characterization

AZTN and GZTN thin films with various Zn:Sn:dopant (Al or Ga) ratios were deposited via pulsed PECVD, and their properties were analyzed using various characterization methods. To confirm the chemical compositions of the films, X-ray photoelectron spectroscopy (XPS, Thermo VG Scientific, Al K-Alpha + X-ray Photoelectron Spectrometer System) and energy-dispersive X-ray spectroscopy (EDS, InLens Detector) were performed. The morphological and structural features of the films were examined via field-emission scanning electron microscopy (FE-SEM, Carl Zeiss, Gemeni 560) and X-ray diffraction (XRD, Rigaku D, MAX-2200). Electrical properties such as the carrier concentration, conductivity, and mobility of the films were characterized via Hall-effect measurements (ECOPIA, HMS-5000). The optical properties, such as the bandgap and energy diagrams, were confirmed by ultraviolet−visible (UV-Vis) spectroscopy (SCINCO, S-4100) and UV photoelectron spectrometry (UPS, NEXGA G2). Finally, the direct-current I-V characteristics of the p-n homojunction devices under ambient conditions (at a temperature of 25 °C) were measured using a semiconductor parameter analyzer (HP4155B), and the C-V characteristics were measured using an LCR meter (Keysight E4980A).

3. Results and discussion

AZTN and GZTN thin films were deposited by alternately injecting Zn/Sn/Al and Zn/Sn/Ga precursors. Fig. 1a shows the sequence and pulse duration of each precursor, the reactant gas, and plasma in a single supercycle of the pulsed PECVD method. During the alternating injection of the Zn precursor (*l* s), Sn precursor (*m* s), and dopant precursor (*n* s), reactant gases N_2 and NH_3 were continuously supplied, and plasma was consistently formed. The process temperature was fixed at 300 °C, and supercycles were repeated until the total deposition time reached 500 s. Dense ZTN films with a smooth surface were deposited at the growth temperature of 300 °C (Fig. S1). In addition, thin films of constant thickness were deposited by fixing the deposition time to 500 s, as shown in Fig. S2 and S3.

As shown in Fig. 1b and c, the atomic concentrations of cations (Zn, Sn, Al, and Ga) in the AZTN and GZTN thin films as a function of the dopant precursor pulse duration were measured using EDS. All the synthesized doped ZTN thin films were fabricated with fixed Zn and Sn injection times of 10 and 6 s, respectively. These injection times afforded undoped ZTN with the highest oxidation resistance and lowest electron carrier concentration [23], making ZTN stable and facilitating its conversion to a p-type semiconductor. The Al content in the AZTN thin films was 4.74, 10.0, 13.0, and 15.9 at% for Al pulse durations of 1, 3, 5, and 7 s, respectively, as shown in Fig. 1b. The Ga content in the GZTN thin

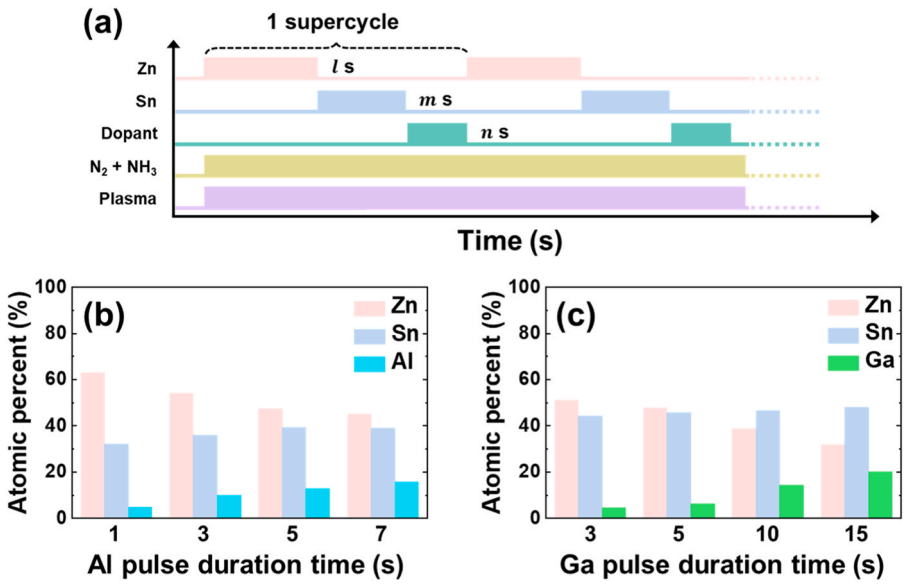

Fig. 1. (a) Schematic of pulse sequence in pulsed PECVD. EDS of (b) AZTN and (c) GZTN thin films. Cation composition of AZTN thin films are depicted for an Al precursor duration time of 1, 3, 5, and 7 s, while those of GZTN thin films are shown for a Ga precursor duration time of 3, 5, 10, and 15 s.

films was 4.57, 6.38, 14.4, and 20.0 at% for Ga pulse durations of 3, 5, 10, and 15 s, respectively, as shown in Fig. 1c. The detailed atomic percentages of all the cations in the AZTN and GZTN thin films with respect to the Al and Ga injection times are presented in Table S1.

The amount of Al and Ga incorporated into ZTN by pulsed PECVD increased linearly with an increase in injection time, as shown in Fig. S4. However, the host materials Zn and Sn exhibited a definite decrease and increase, respectively, even though the Zn and Sn precursor injection times remained unchanged. This is attributed to the interplay of precursor volatility and reactivity. Volatile precursors, such as DEZ (~100 Torr @ 20 °C), exhibit a high propensity to saturate the reaction surface quickly owing to their low boiling points and rapid desorption kinetics. This saturation limits their incorporation efficiency when competing precursors with lower volatility, such as TDMASn (~0.008 Torr @ 20 °C), TMA (~11 Torr @ 20 °C), or $C_5H_{13}OGa$ (~0.1 Torr @ 20 °C), are introduced [34].

In comparison, less volatile precursors, such as TDMASn, exhibit prolonged surface residency times, enabling more extensive surface reactions and higher incorporation rates. The differential incorporation behaviors of Zn and Sn are governed by the thermodynamic and kinetic competition between precursors. This competition alters the energy barriers for adsorption, desorption, and subsequent chemical reactions, favoring the inclusion of less volatile species over more volatile ones under the same reaction conditions. The kinetic energy available at the surface plays a pivotal role in facilitating or hindering specific reaction pathways, as higher energy environments may enhance precursor reactivity but also promote the desorption of highly volatile species. This interplay governs the observed concentration changes and underscores the complexity of CVD processes [35–37].

In this context, Olsen et al. reported that in ZTN, which has an orthorhombic structure, the formation energy decreased when Al and Ga replaced the Zn sites instead of the Sn sites [19]. Because of this low formation energy, it may be preferable to substitute the dopant material (Al and Ga) with a Zn host material. However, XRD analysis revealed that the doped ZTN manufactured in this study had an amorphous phase, as shown in Fig. S5. In addition, selected-area electron diffraction patterns obtained using a transmission electron microscope confirmed that the deposited thin films were amorphous, with no nanocrystalline structure (Fig. S6). Determining the mechanisms underlying these behaviors in amorphous materials is not easy, because amorphous materials have more irregularities than crystalline structures, making their behavior less predictable and more difficult to model. Theoretical calculations, e.g., density functional theory, are expected to provide insights into the thermodynamic and kinetic changes, as well as the reaction energies, that influence these behaviors. These findings highlight the complexity of amorphous ZTN systems and emphasize the need for combined experimental and computational studies to clarify the dopant substitution mechanisms and optimize material performance.

Fig. 2 presents the XPS core-level spectra of AZTN and GZTN at various concentrations of Al and Ga, providing insights into how doping influences the chemical environment within the amorphous ZTN thin film. The XPS spectra were analyzed with vertical emission geometry using conventional monochromatic Al Kα radiation ($h\nu$ = 1486.6 eV). The pass energy of the XPS spectra was kept at 50.0 eV. To remove surface contamination, a 10-s Ar^+ sputtering process was performed.

For AZTN, the Al 2p core-level spectrum shown in Fig. 2a reveals that as the concentration of Al increased, the intensity of the Al-N peak (73.1 eV) increased without a shift in the peak position [38,39]. This suggests that Al does not act as a substitutional dopant but instead affects the local bonding environment. Simultaneously, Zn $2p_{3/2}$ spectrum (Fig. 2c) shows a reduction in the intensity of the Zn interstitial (Zn_i) peak (~1021.0 eV) coupled with a more pronounced Zn-N bonding peak at a higher binding energy (~1021.2 eV) as the Al concentration increases [21,40]. These findings indicate that excessive Al doping can stabilize the Zn atomic environment by mitigating the formation of Zn_i defects, potentially through local bonding rearrangements. Additionally, the Sn $3d_{5/2}$ spectrum (Fig. 2d) reveals a decline in the interstitial Sn (Sn_i) peak (~484.1 eV), while the Sn^{2+} (484.8 eV) and Sn^{4+} (485.5 eV) peaks become more pronounced [28]. These changes demonstrate that Al doping plays a role in stabilizing the oxidation states of Sn, potentially by modifying the local defect landscape and reducing the amount of unstable interstitial Sn species [41]. These effects may be related to changes in the local electronic environment, which may influence the oxidation-state distribution of Zn and Sn within the amorphous network [42].

In Fig. 2e, the N 1 s spectra support these findings. The peak corresponding to Sn-N bonding (397.2 eV) has a high binding energy owing to the high electronegativity of Sn [11,39], whereas that corresponding to Zn-N bonding (396.2 eV) is observed at a lower binding energy [22]. Because the electronegativity of Al is similar to that of Zn, as the Al concentration increased, the relative intensity of the Al-N (and Zn-N) bonding peak compared to that of Sn-N increased. Additionally, the

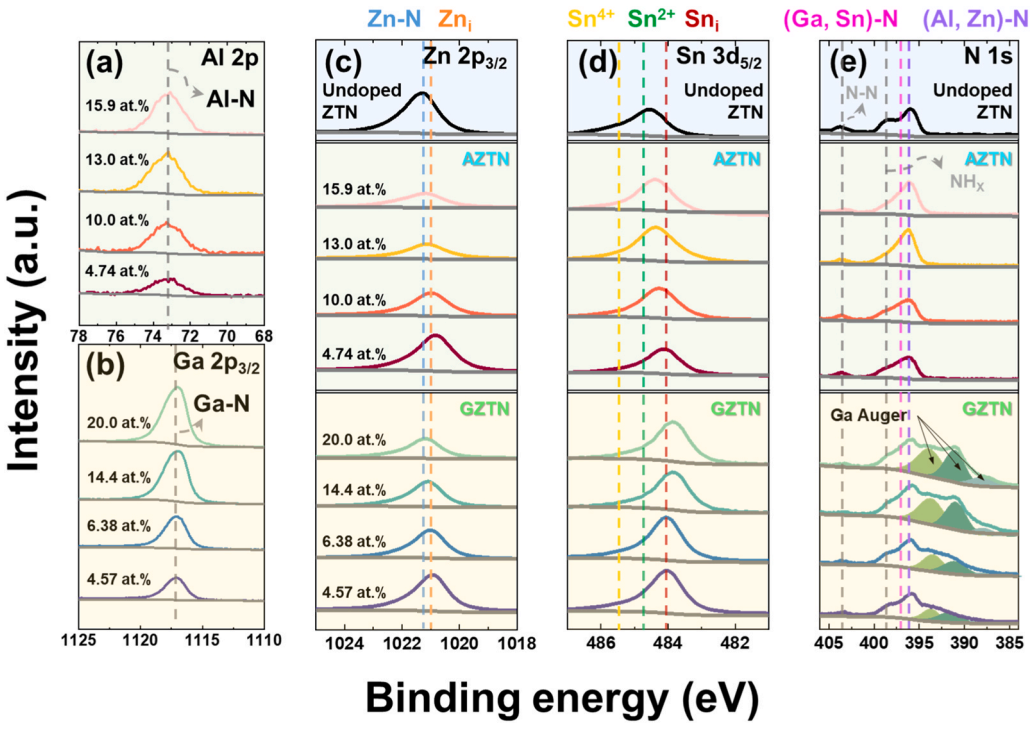

Fig. 2. XPS spectra according to dopant concentration of (a) Al 2p, (b) Ga 2p$_{3/2}$, (c) Zn 2p$_{3/2}$, (d) Sn 3d$_{5/2}$ and (e) N 1 s core levels of AZTN and GZTN with undoped ZTN for comparison.

NH_x free amine peak (398.8 eV) and N-N peak (403.3 eV) commonly observed for nitrides synthesized using PECVD with N_2 and NH_3 plasma emerged in the spectrum [43–49]. However, their correlation with Al doping remains unclear, suggesting that they may primarily result from the PECVD process rather than direct doping effects.

Al and Ga doping exhibited different effects on the ZTN thin film. In the Ga 2p$_{3/2}$ spectrum (Fig. 2b), the intensity of the Ga-N bonding peak (1117.1 eV) increases proportionally with the Ga concentration without a significant shift in binding energy, indicating a stable Ga-N bonding environment [43]. As shown in Fig. 2c, increasing the Ga concentration reduces the Zn$_i$ peak intensity and shifts the Zn 2p$_{3/2}$ peak to higher binding energies, signifying enhanced Zn-N bonding and reduced Zn$_i$ defects. In the Sn 3d$_{5/2}$ spectrum (Fig. 2d), a different trend is observed: the Sn$_i$ peak intensity increases significantly at Ga concentrations above 14.4 at%. This behavior is attributed to a reduced Zn concentration in the amorphous network, likely due to process-related effects where extended Ga precursor injection limits Zn incorporation. The increased relative abundance of Sn promotes Sn$_i$ defect formation, underscoring the complex interplay between Ga doping and the amorphous ZTN [28].

The N 1 s spectrum (Fig. 2e) reveals additional effects of Ga doping. An increase in Ga-Auger peaks and Ga-N peak intensity (~397.4 eV) is observed with increasing Ga concentration, indicating reinforced Ga-N bonding interactions [50,51]. In addition, owing to the similar electronegativities of Ga and Sn, the Ga-N binding energy in the N 1 s spectrum could be similar to that of Sn-N, making it challenging to distinguish between the two interactions. As a result, the N 1 s binding energy remained relatively constant, and the incorporation of Ga contributed to Ga-N bonding interactions.

The XPS analysis indicated that Al and Ga doping do not clearly exhibit direct substitution of Zn or Sn but rather influence the defect chemistry and bonding environment of the amorphous ZTN network. At lower dopant concentrations, Al and Ga doping both significantly affect the bonding environment compared with undoped ZTN. As the dopant concentration increases, dopant-N and Zn-N bond interactions are enhanced, shifting to a binding state similar to that of undoped ZTN, as evidenced by shifts in binding energy. However, the effect of Ga doping on Sn bonding interactions seems to become more complex, while Al doping still appears to be effective for reducing interstitial defects and stabilizing the amorphous network. Thus, the observed difference in binding energy between the doped and undoped ZTN films indicates that doping plays a crucial role in modulating the electronic structure and influencing the electrical properties of the material. These findings emphasize the critical role of defect engineering in achieving p-type conductivity in amorphous materials and provide a deeper understanding of how dopant incorporation affects the structural and electronic properties of ZTN thin films.

Hall-effect measurements were employed to estimate the electrical properties, such as the carrier concentration, mobility, and conductivity, of the AZTN and GZTN thin films. Measurements were performed at room temperature, and the reproducibility of the samples was confirmed by analyzing the characteristics of multiple batches obtained under identical conditions and representing the results with error bars. Specifically, square-shaped samples were prepared with electrical contacts at the four corners using a 4-point probe method. Hall voltage was measured under a magnetic field of 0.54 T while controlling the current. Using the Van der Pauw method, carrier concentration was calculated from the measured Hall voltage. The sheet resistance was also measured using the 4-point probe technique, and conductivity σ was calculated by dividing the reciprocal of R_s by the film thickness d. Finally, the mobility μ was determined using the relation $\mu = \sigma/(qn)$, where q is the elementary charge and n is the carrier concentration obtained from the Hall measurement [52–54]. In previous studies, the majority of undoped ZTN thin films exhibited n-type conductivity. In particular, undoped ZTN exhibits electron concentrations of ~10^{13}–10^{19} cm^{-3}, a mobility of ~1–10 cm^2/(V•s), and a conductivity of ~10^{-4}–1 S•cm^{-1} depending on the composition [23]. However, in Fig. 3, the doped ZTN thin films exhibit p-type conductivity. AZTN exhibits (a) hole concentrations ranging from approximately 10^{14}–10^{18} cm^{-3}, (b) hole mobilities of ~1–10 cm^2/(V•s), and (c) p-type conductivity of ~10^{-1}–10^{-4} S•cm^{-1}, varying with the Al concentration. GZTN exhibits (a) hole concentrations ranging from 10^{13} to 10^{17} cm^{-3}, (b) hole mobilities of ~1–10 cm^2/(V•s), and (c) p-type conductivity of ~10^{-2}–10^{-5} S•cm^{-1},

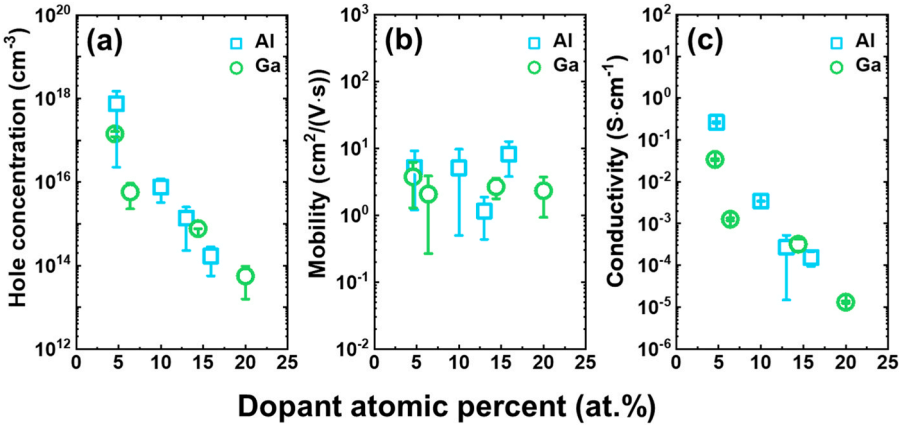

Fig. 3. Hall-effect measurements of AZTN and GZTN thin films according to dopant concentration. Electrical properties (a) hole concentration, (b) mobility and (c) conductivity are shown. The blue dots in each figure represent the results of AZTN thin films and lime green dots represent those of GZTN thin films.

depending on the Ga concentration. Thus, the carrier concentration decreases as the dopant concentration increases [55,56]. This phenomenon appears to be closely associated with alterations in the bonding environment of the amorphous ZTN network induced by Al and Ga doping, as well as variations in dopant concentration, as evidenced by the XPS core-level spectra presented in Fig. 2.

Typically, Zn interstitial defects are expected to reduce the p-type conductivity by acting as donor defects. However, in the amorphous ZTN phase, Al or Ga doping can promote the formation of localized Zn_i defects, which may lead to the creation of shallower acceptor levels through defect complex formation, rather than allowing Zn_i to function as an independent donor [57]. Similarly, p-type doping studies of ZnO have demonstrated that doping can alter the formation energies of multiple defects and facilitate the formation of defect complexes [58,59]. Additionally, the introduction of Al and Ga may stabilize donor-like defects or complexes via interaction with Zn_i. This stabilization reduces the donor activity of Zn_i and can increase the hole concentration in the valence band, increasing the p-type conductivity. The formation energy of Zn_i-related acceptor levels depends on not only the dopant concentration and the chemical potential conditions during synthesis but also the composition and bonding environment of the ZTN thin film [17]. Consequently, increasing the doping concentrations of Al and Ga reduced the hole concentration in the doped ZTN thin films [60].

The combination of Hall-effect measurements and XPS analyses reveals that doping-induced modifications in the defect chemistry and bonding environment significantly affect the electrical properties of

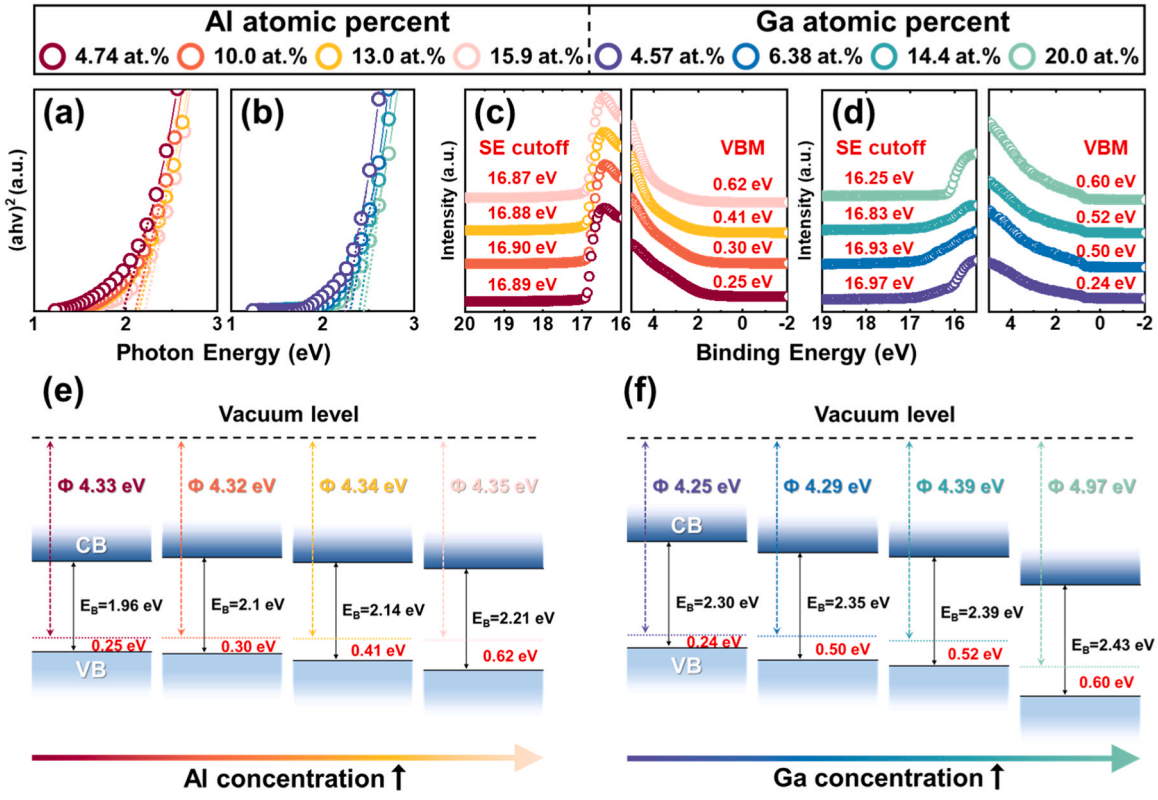

Fig. 4. UV-Vis Tauc plots of (a) AZTN and (b) GZTN thin films according to dopant concentration. Optical band gaps are estimated by x-axis intersection points of each tangent line. UPS spectra of (c) AZTN and (d) GZTN thin films are shown with SE cutoff energy and VBM energy with the Fermi level set at 0 eV. Schematic band diagrams of (e) AZTN and (f) GZTN thin films constructed with values obtained from (a) to (d).

amorphous ZTN thin films. Despite the observed trends, the exact mechanisms governing the defect behavior in the amorphous ZTN phase remain unclear. In contrast to crystalline materials, amorphous systems exhibit highly localized electronic states and irregular bonding environments, complicating the defect dynamics and their impact on electrical properties. These complexities demonstrate the challenges of defect engineering in amorphous materials and highlight the need for further investigations into the formation energies, defect interactions, and chemical potential conditions that determine the defect landscape in amorphous systems.

A Tauc plot was used to calculate the optical bandgaps of the amorphous-doped ZTN semiconductors. In Fig. 4a and b, the optical bandgaps of the AZTN and GZTN thin films increase with the dopant concentration. The observed bandgap widening can be generally understood in the context of Vegard's law, which predicts that the bandgap of an alloy system (or mixed crystal) varies with composition [61,62]. Considering that AlN (~6.2 eV) and GaN (~3.4 eV) have larger bandgaps than ZTN (~2.7 eV), the incorporation of Al and Ga into ZTN is expected to increase the overall bandgap [63,64]. However, since the ZTN films are amorphous, the precise application of Vegard's law is limited. Amorphous materials exhibit some order but lack a clearly defined structure. The extended electronic states of crystalline materials can result in distinct energy bands. In contrast to their crystalline counterparts, the absence of periodicity in amorphous materials stimulates significant changes in their electrical environments, leading to localized states arising from disruptions in the energy band structure due to disordered atomic positions. This structural disruption influences the integration of dopant elements into the amorphous ZTN network and ultimately affects the optical properties.

The incorporation of Al and Ga into the amorphous ZTN involves distinct interactions compared with Zn and Sn, owing to differences in their ability to form covalent bonds with nitrogen. As the dopant concentration increases, dopant atoms are more effectively incorporated into the amorphous ZTN system, leading to a reduction in defects such as Zn interstitials and a subsequent decrease in hole concentration, as illustrated in Figs. 2 and 3. The reduction and compensation of defects result in a lower density of mid-gap trap states and facilitate the formation of a more distinct and well-defined band structure, contributing to bandgap widening [65].

Under Sn-rich conditions, higher Sn_i defect concentrations are observed because of the increased Sn content, but these defects do not appear to significantly impact the optical properties. This observation is consistent with the Hall-effect measurement, where Sn_i defects do not seem to cause notable changes in the bandgap, likely owing to charge-compensation mechanisms such as the redistribution of electronic density around Zn and Sn sites, which mitigate the effects of interstitial defects. This reorganization of local bonding environments minimizes defect contributions to the bandgap and supports bandgap widening [66].

UPS measurements were performed using a He I photon source ($h\nu$ = 21.22 eV). Fig. 4c and d show the UPS spectra of AZTN and GZTN, respectively. We evaluated the effects of Al and Ga doping on the electrical structure of ZTN, with a focus on the energies of the secondary electron (SE) cutoff and the valence-band maximum (VBM). Fig. 4c presents the results of the UPS measurements performed on doped ZTN with various concentrations of Al. The work function was calculated by subtracting the energy of the SE cutoff from the energy of the applied photon source ($\Phi = 21.22 - E_{cutoff}$). The work-function energies of the AZTN thin films with Al concentrations of 15.9, 13.0, 10.0, and 4.7 at% were 4.35, 4.34, 4.32, and 4.33 eV, respectively. The VBM energies decreased from 0.62 to 0.25 eV as the Al concentration decreased from 15.9 to 4.74 at%. The gradual increase in the gap between the VBM and Fermi level energies indicates that the addition of Al as a dopant reduces the concentration of holes. The decrease in hole concentration with increasing Al content is attributed to the creation of defect states that function as hole traps or to a shift in the Fermi level toward the conduction band, which reduces the number of holes.

Fig. 4d shows the SE cutoff energy used to calculate the work function and VBM energy position, which depend on the Ga concentration in GZTN. The work functions of the GZTN thin films with Ga concentrations of 20.0, 14.4, 6.38, and 4.57 at% were determined via the same method used for AZTN. The work-function energies of GZTN were calculated to be 4.97, 4.39, 4.29, and 4.25 eV, respectively. The VBM energies of the GZTN thin films are 0.60, 0.52, 0.50, and 0.24 eV lower than the Fermi level.

The work function and VBM energy positions depend on the dopant concentration, as shown in Fig. 4c and d, and the bandgap values are presented in Fig. 4a and b. Using this information, we estimated the band structures of the AZTN and GZTN thin films, as illustrated in Fig. 4e and f. As the doping concentrations of Al and Ga increased, the work function increased, and the gap between the VBM and the Fermi level widened. Interestingly, this finding correlates well with the Hall-effect measurements, which indicated that higher levels of doping caused the Fermi level to rise closer to the conduction band. In other words, as the dopant concentration increases, the density of the shallow states decreases, reducing the hole concentration and consequently pushing the Fermi level farther from the valence band.

The performance of p-n homojunction devices composed of n-ZTN (undoped ZTN) and p-ZTN (AZTN and GZTN thin films) was evaluated. A schematic of the device with an optical image of the top electrode is shown in Fig. 5d. Additionally, FE-SEM cross-sectional images of the devices composed of AZTN and GZTN are shown in Fig. 5c and e, respectively. In these images, there are no discernible boundaries at the interface, and the thickness is uniform.

Fig. 5a, b, and the insets show the I-V characteristics and rectification ratio (RR) of the p-n junction diode. The rectification ratio is defined as the ratio of the forward current to the reverse current, typically measured at the same magnitude of forward and reverse bias voltages. Overall, both devices composed of AZTN and GZTN thin films forming the p-n homojunction exhibited good rectifying characteristics. The forward current of the AZTN/n-ZTN thin-film devices increased to ~80 mA with increasing hole concentration because of the decreasing Al concentration. The forward current of the GZTN devices exhibited a tendency similar to that of the AZTN thin-film devices, increasing to ~60 mA.

The difference between the forward and reverse currents in the I-V curve was used to calculate the RR ($|I_{F(max)}|/|I_{R(max)}|$) values. The RR values of the AZTN devices decreased from 60 to 7 with increasing Al concentration. For the GZTN devices, the RR decreased from 200 to 20 with decreasing Ga concentration. The maximum RR value was observed for 4.74 at% Al in AZTN and 20.0 at% Ga in GZTN. Because n- and p-type semiconductors form junctions, the I-V characteristics and RR values are affected by the built-in potential (V_{bi}) generated at these junctions. The V_{bi} of a p-n junction is determined by the difference in the Fermi levels of the n- and p-type semiconductors in the thermal equilibrium state.

To investigate the variations in V_{bi} of p-ZTN and n-ZTN as influenced by the dopant concentration, the band structure of n-ZTN was systematically explored. Fig. S7a and b show that the gap between the Fermi level and VBM is 1.68 eV with bandgap of 1.72 eV, and the work function is 4.01 eV. The gap in the Fermi level between AZTN and n-ZTN based on the Al concentration in the AZTN ranges from 0.31 to 0.34 eV. In addition, the difference in Fermi level between GZTN and n-ZTN, which depends on the Ga concentration, ranges from 0.24 to 0.96 eV. In AZTN/n-ZTN devices, the variation in Fermi level energy with respect to the Al concentration was found to be < 0.03 eV. Nevertheless, the devices exhibited excellent rectification characteristics because the potential was also influenced by the carrier concentration, which affected the depletion width. The depletion region, which is a crucial part of a junction diode, was confirmed using C-V measurements.

Capacitance measurements in semiconductor devices, such as p-n junctions, can be significantly affected by the series resistance—partic-

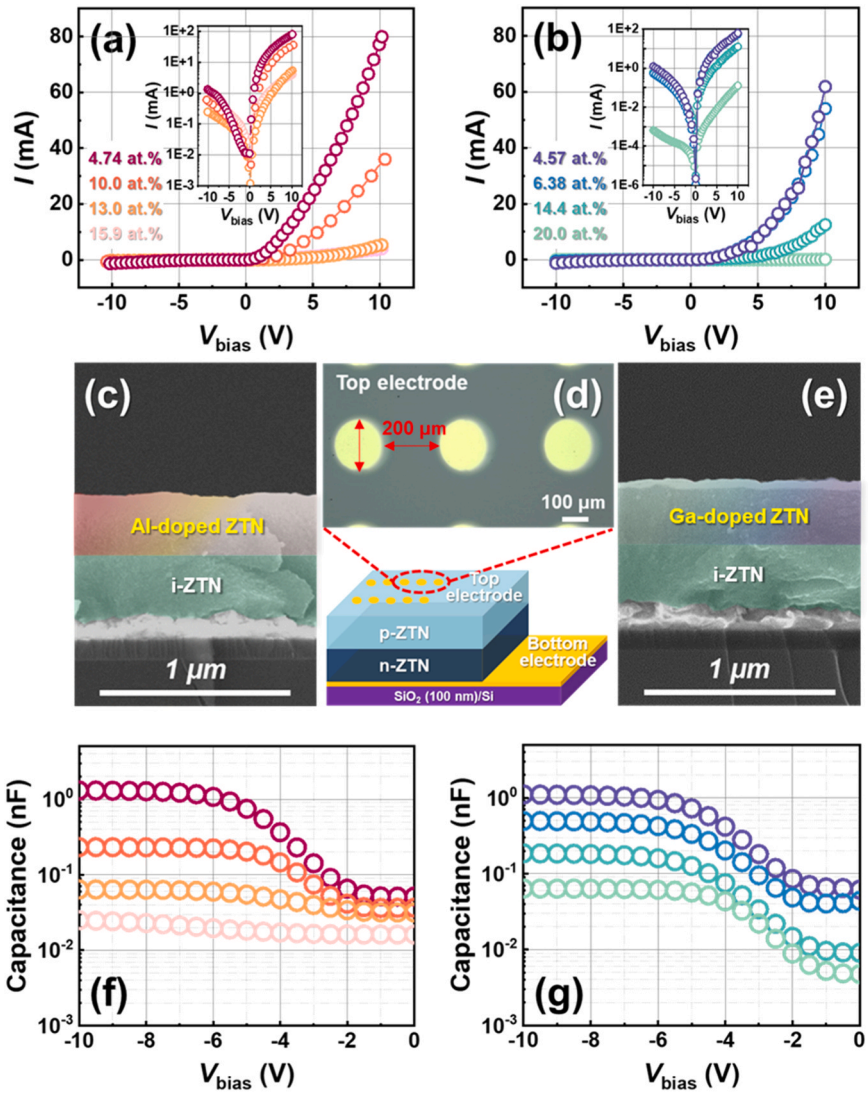

Fig. 5. Performance of p-n homojunction devices according to dopant concentration. I-V curves of (a) AZTN/n-ZTN and (b) GZTN/n-ZTN thin-film devices depicted in a linear scale. Insets are I-V curves of each device in semi-log scale to obtain the RR values. FE-SEM cross-sectional images of (c) AZTN/n-ZTN and (e) GZTN/n-ZTN thin-film devices. (d) Schematic of device structure with optical microscope image of top electrodes. C-V characteristics of (f) AZTN/n-ZTN and (g) GZTN/n-ZTN thin-film devices.

ularly at high frequencies. To determine the true capacitance accurately, it is necessary to correct the measured capacitance by accounting for the series resistance of p-ZTN. The series resistance of p-ZTN varied with the dopant concentration, as shown in Fig. 3. In our study, the series resistance was measured via the four-point probe method, and the capacitance of the p-n junction device was determined at 1.0 MHz at room temperature. We used a correction formula to eliminate the contribution of the series resistance to the measured capacitance [4,67]:

$$C_{true} = \frac{C_{measure}}{\sqrt{1 + (\omega R_S C_{measure})^2}} \quad (1)$$

In Eq. (1), $\omega = 2\pi f$ represents the angular frequency (with f=1 MHz), R_S represents the series resistance measured, $C_{measure}$ represents the capacitance measured at 1 MHz, and C_{true} represents the corrected capacitance that excludes the effect of the series resistance. This formula is derived according to the principle that the impedance (Z) of a capacitive system with a series resistance can be expressed as:

$$Z = R_S + \frac{1}{j\omega C} \quad (2)$$

The correction formula considers the frequency-dependent effects of the series resistance and provides the true capacitance of the p-n junction. The corrected true capacitances are presented in Fig. 5f and g. As shown in Fig. 5f, for the AZTN/n-ZTN thin film device, as the Al concentration in AZTN decreased, higher capacitance values were obtained at the same bias voltage. Similarly, in Fig. 5g, for the GZTN/n-ZTN thin film device, higher capacitance values are observed at the same voltage as the Ga concentration decreases. Furthermore, for both devices, as the applied negative voltage increases, the capacitance values saturate.

When the electron concentration in n-ZTN remains constant, an increase in the hole concentration in the doped ZTN reduces the depletion width. As the depletion width decreases, V_{bi} decreases, facilitating diffusion and drift for both holes and electrons. Therefore, the increasing RR values were caused by the increase in the hole concentration of the doped ZTN, leading to higher forward current flow under the same forward bias [68]. Notably, the main reason for GZTN samples with a Ga concentration of 20.0 at% exhibiting the highest RR value among all the samples was the far higher Fermi level gap energy between the n-type ZTN and GZTN, along with an expanded depletion width. Overall, the Al and Ga concentrations significantly affected the electrical characteristics of p-ZTN, influencing device performance. These results highlight that

both dopant concentration and type are critical for modifying ZTN-based semiconductors and optimizing junction diode performance, particularly because depletion-region dynamics play a crucial role. The findings further confirm the unprecedented achievement of a ZTN-based p-n homojunction device, demonstrating rectifying characteristics over a range of dopant concentrations. Such devices are particularly promising for optoelectronic applications, including PV and PEC devices, where precise control of carrier concentration and rectifying characteristics is required. Moreover, by analyzing how Al and Ga concentrations affect material properties and device performance, we show that materials can be tailored to meet specific application requirements. This study is expected to drive groundbreaking advancements in nitride-based applications, bringing the field closer to fully realizing its potential.

4. Conclusions

In this study, we fabricated and characterized the first p-n homojunction device using doped ZTN thin films synthesized by pulsed PECVD with varying Al and Ga concentrations. Al and Ga doping significantly influenced the electrical and optical properties, with Hall-effect measurements confirming p-type conductivity, featuring hole concentrations from $\sim10^{13}$ to $\sim10^{18}$ cm^{-3} and mobilities between 1 and 10 $cm^2/(V{\cdot}s)$. Dopant-induced Zn and Sn interstitial defects contributed to enhanced p-type behavior, though the exact conduction mechanisms remain unclear. UV-Vis and UPS analyses showed that the dopant concentration affected the bandgap (4.25–4.97 eV), work function, and Fermi level. This work demonstrates controlled p-type doping in amorphous ZTN, expanding its application potential and laying groundwork for future ternary nitride semiconductor devices.

CRediT authorship contribution statement

Nameun Kim: Writing – review & editing, Writing – original draft, Investigation, Formal analysis, Data curation. **Ji Woon Choi:** Writing – review & editing, Writing – original draft, Methodology, Investigation, Formal analysis, Data curation. **Wooseok Song:** Investigation, Formal analysis, Data curation. **Saewon Kang:** Validation, Supervision, Resources, Funding acquisition. **Ki-Seok An:** Validation, Supervision, Resources, Methodology, Funding acquisition, Conceptualization. **Taek-Mo Chung:** Funding acquisition. **Soonmin Yim:** Validation, Supervision, Resources, Funding acquisition. **Jung-Woo Yoo:** Supervision.

Declaration of Competing Interest

The authors declare that they have no known competing financial interests or personal relationships that could have appeared to influence the work reported in this paper.

Acknowledgments

This research was supported by the National Research Foundation of Korea (NRF) funded by the Ministry of Science and ICT (2022M3H4A3085259, 2020M3H4A3081866) and by the Development of Smart Chemical Materials for IoT Devices Project (KS2521-10) through the Korea Research Institute of Chemical Technology.

Appendix A. Supporting information

Supplementary data associated with this article can be found in the online version at doi:10.1016/j.jallcom.2025.183625.

References

[1] L. Sang, M. Liao, B. Shen, AlN as interlayer for effective thermal dissipation from gallium nitride to CVD diamond using nanocrystalline diamond seeding, Inf. Funct. Mater. 1 (2024) 331–337.
[2] Q. Lei, L. Li, W. Lu, J. Tao, R. Ling, L. Zhang, X. Chen, S. Wu, S. Li, S. Li, Preparation and research progress of GaN-based avalanche photodetectors, Microstructures 5 (2025) (N/A-N/A).
[3] Q. Liu, J. Shi, W. Song, X. Wang, L. He, S. Zhan, F. Gao, S. Li, Fowler-nordheim tunneling mechanism Graphene/GaN ultraviolet position-sensitive detector with high precision for optoelectronic demodulation applications, J. Alloy. Compd. 960 (2023) 170712.
[4] S.M. Sze, Y. Li, K.K. Ng, Physics of Semiconductor Devices, John wiley & sons, 2021.
[5] S. Dimitrijev. MOSFET, Principles of Semiconductor Devices, second ed., Oxford University Press, New York, NY, USA, 2012, pp. 470–472.
[6] D.A. Neamen, D. Biswas, Semiconductor Physics and Devices, McGraw-Hill higher education, New York, 2011.
[7] J.M. Shah, Y.-L. Li, T. Gessmann, E.F. Schubert, Experimental analysis and theoretical model for anomalously high ideality factors (n≫ 2.0) in AlGaN/GaN pn junction diodes, J. Appl. Phys. 94 (2003) 2627–2630.
[8] A.L. Greenaway, C.L. Melamed, M.B. Tellekamp, R. Woods-Robinson, E.S. Toberer, J.R. Neilson, A.C. Tamboli, Ternary nitride materials: fundamentals and emerging device applications, Annu. Rev. Mater. Res. 51 (2021) 591–618.
[9] W. Sun, C.J. Bartel, E. Arca, S.R. Bauers, B. Matthews, B. Orvananos, B.R. Chen, M. F. Toney, L.T. Schelhas, W. Tumas, J. Tate, A. Zakutayev, S. Lany, A.M. Holder, G. Ceder, A map of the inorganic ternary metal nitrides, Nat. Mater. 18 (2019) 732–739.
[10] S.R. Bauers, A. Holder, W. Sun, C.L. Melamed, R. Woods-Robinson, J. Mangum, J. Perkins, W. Tumas, B. Gorman, A. Tamboli, G. Ceder, S. Lany, A. Zakutayev, Ternary nitride semiconductors in the rocksalt crystal structure, Proc. Natl. Acad. Sci. USA 116 (2019) 14829–14834.
[11] E. Lewin, J. Patscheider, Structure and properties of sputter-deposited Al-Sn-N thin films, J. Alloy. Compd. 682 (2016) 42–51.
[12] A. Zakutayev, Synthesis of Zn_2NbN_3 ternary nitride semiconductor with wurtzite-derived crystal structure, J. Phys. Condens Matter 33 (2021).
[13] I.S. Khan, K.N. Heinselman, A. Zakutayev, Review of $ZnSnN_2$ semiconductor material, J. Phys. Energy 2 (2020).
[14] A. Zakutayev, C.M. Caskey, A.N. Fioretti, D.S. Ginley, J. Vidal, V. Stevanovic, E. Tea, S. Lany, Defect tolerant semiconductors for solar energy conversion, J. Phys. Chem. Lett. 5 (2014) 1117–1125.
[15] H. Zeng, Y. Wen, L. Yin, R. Cheng, H. Wang, C. Liu, J. He, Recent developments in CVD growth and applications of 2D transition metal dichalcogenides, Front. Phys. 18 (2023) 53603.
[16] F. Gao, Z. Li, S. Li, Recent advances in the preparation of Gallium-based 2D materials and devices based on gallium liquid metal, Adv. Funct. Mater. (2025) 2424370.
[17] S. Chen, P. Narang, H.A. Atwater, L.W. Wang, Phase stability and defect physics of a ternary $ZnSnN_2$ semiconductor: first principles insights, Adv. Mater. 26 (2014) 311–315.
[18] N. Tsunoda, Y. Kumagai, A. Takahashi, F. Oba, Electrically benign defect behavior in zinc tin nitride revealed from first principles, Phys. Rev. Appl. 10 (2018).
[19] V.S. Olsen, Y.K. Frodason, Y.K. Hommedal, D.M. Nielsen, P.M. Weiser, K.M. H. Johansen, I.-H. Lee, A.Y. Kuznetsov, L. Vines, Li and group-III impurity doping in $ZnSnN_2$: potential and limitations, Phys. Rev. Mater. 6 (2022).
[20] N.L. Adamski, Z. Zhu, D. Wickramaratne, C.G. Van de Walle, Strategies for p-type doping of $ZnGeN_2$, Appl. Phys. Lett. 114 (2019).
[21] Kk Chinnakutti, L. Patra, V. Panneerselvam, D. Govindarajan, S. Kheawhom, J. Theerthagiri, Y. Yu, S.T. Salammal, M.Y. Choi, Lithium inserted $ZnSnN_2$ thin films for solar absorber: n to p-type conversion, materials today, Chemistry 25 (2022).
[22] Kk Chinnakutti, V. Panneerselvam, S.Thankaraj Salammal, Ba-acceptor doping in $ZnSnN_2$ by reactive RF magnetron sputtering: (002) faceted Ba–$ZnSnN_2$ films, J. Alloy. Compd. 855 (2021).
[23] J.W. Choi, J. Kim, S.R. Pae, J. Kim, C.G. Kim, H. Lee, S. Ji, S.-W. Nam, Y.K. Lee, B. Shin, Oxidation-Resistant amorphous zinc tin nitride films with tunable optical and electrical properties, Chem. Mater. 34 (2022) 6802–6808.
[24] Y. Wang, T. Ohsawa, X. Meng, F. Alnjiman, J.-F. Pierson, N. Ohashi, Suppressing the carrier concentration of zinc tin nitride thin films by excess zinc content and low temperature growth, Appl. Phys. Lett. 115 (2019).
[25] Kk Chinnakutti, V. Panneerselvam, S.Thankaraj Salammal, Tailoring optoelectronic properties of earth abundant $ZnSnN_2$ by combinatorial RF magnetron sputtering, J. Alloy. Compd. 772 (2019) 348–358.
[26] F. Alnjiman, S. Diliberto, J. Ghanbaja, E. Haye, S. Kassavetis, P. Patsalas, C. Gendarme, S. Bruyère, F. Cleymand, P. Miska, P. Boulet, J.F. Pierson, Chemical environment and functional properties of highly crystalline $ZnSnN_2$ thin films deposited by reactive sputtering at room temperature, Sol. Energy Mater. Sol. Cells 182 (2018) 30–36.
[27] A.N. Fioretti, A. Zakutayev, H. Moutinho, C. Melamed, J.D. Perkins, A.G. Norman, M. Al-Jassim, E.S. Toberer, A.C. Tamboli, Combinatorial insights into doping control and transport properties of zinc tin nitride, J. Mater. Chem. C. 3 (2015) 11017–11028.
[28] X. Wu, F. Meng, D. Chu, M. Yao, K. Guan, D. Zhang, J. Meng, Carrier tuning in $ZnSnN_2$ by forming amorphous and microcrystalline phases, Inorg. Chem. 58 (2019) 8480–8485.

[29] N. Feldberg, J.D. Aldous, W.M. Linhart, L.J. Phillips, K. Durose, P.A. Stampe, R. J. Kennedy, D.O. Scanlon, G. Vardar, R.L. Field, T.Y. Jen, R.S. Goldman, T.D. Veal, S.M. Durbin, Growth, disorder, and physical properties of $ZnSnN_2$, Appl. Phys. Lett. 103 (2013).

[30] K. Javaid, W. Wu, J. Wang, J. Fang, H. Zhang, J. Gao, F. Zhuge, L. Liang, H. Cao, Band offset engineering in $ZnSnN_2$-Based heterojunction for Low-Cost solar cells, ACS Photonics 5 (2018) 2094–2099.

[31] F. Kawamura, N. Yamada, M. Imai, T. Taniguchi, Synthesis of $ZnSnN_2$ crystals via a high-pressure metathesis reaction, Cryst. Res. Technol. 51 (2016) 220–224.

[32] G. Cinti, V. Liso, S.L. Sahlin, S.S. Araya, System design and modeling of a high temperature PEM fuel cell operated with ammonia as a fuel, Energies 13 (2020).

[33] S.R. Droes, T.T. Kodas, M.J. Hampden-Smith, Plasma-enhanced chemical vapor deposition (PECVD). Carbide, Nitride and Boride Materials Synthesis and Processing, Springer, 1997, pp. 579–603.

[34] Y. Xu, X.-T. Yan, Thermodynamics and kinetics of chemical vapour deposition, Chem. Vap. Depos. Integr. Eng. Des. Adv. Mater. (2010) 129–164.

[35] R.W. Johnson, A. Hultqvist, S.F. Bent, A brief review of atomic layer deposition: from fundamentals to applications, Mater. Today 17 (2014) 236–246.

[36] K. Choy, Chemical vapour deposition of coatings, Prog. Mater. Sci. 48 (2003) 57–170.

[37] Y. Tian, Z. Yan, L. Jiang, R. Liu, B. Liu, Y. Shao, X. Yang, M. Liu, Multiscale models of CVD process: review and prospective, Materials 17 (2024) 5131.

[38] C. Ozgit-Akgun, E. Goldenberg, A.K. Okyay, N. Biyikli, Hollow cathode plasma-assisted atomic layer deposition of crystalline AlN, GaN and $Al_xGa_{1-x}N$ thin films at low temperatures, J. Mater. Chem. C. 2 (2014) 2123–2136.

[39] Y.S. Liu, C.I. Hsieh, Y.J. Wu, Y.S. Wei, P.M. Lee, C.Y. Liu, Transparent p-type AlN:SnO_2 and p-AlN:SnO_2/n-SnO_2:In_2O_3 p-n junction fabrication, Appl. Phys. Lett. (2012) 101.

[40] M. Doosti, R. Jahanshahi, S. Laleh, S. Sobhani, J.M. Sansano, Solar light induced photocatalytic degradation of tetracycline in the presence of ZnO/$NiFe_2O_4$/Co_3O_4 as a new and highly efficient magnetically separable photocatalyst, Front. Chem. 10 (2022) 1013349.

[41] L. Guo, Q. Wang, C. Wang, X. Chu, Y. Hao, Y. Chi, X. Yang, Effect of ga doping on the stability and optoelectronic properties of ZnSnO thin film transistor, Micromachines 15 (2024) 1445.

[42] S. Aikawa, T. Nabatame, K. Tsukagoshi, Effects of dopants in InO_x-based amorphous oxide semiconductors for thin-film transistor applications, Appl. Phys. Lett. 103 (2013).

[43] M. Kumar, A. Kumar, S.B. Thapa, S. Christiansen, R. Singh, XPS study of triangular GaN nano/micro-needles grown by MOCVD technique, Mater. Sci. Eng. B 186 (2014) 89–93.

[44] M. GrodzickiProperties of Thin Film-Covered GaN(0001) Surfaces, In: Proceedings of the 2nd Coatings and Interfaces Web Conference (CIWC-2 2020)2020.

[45] Y.-J. Lin, Y.-M. Chen, T.-J. Cheng, Schottky barrier height and nitrogen–vacancy-related defects in ti alloyed ohmic contacts to n-GaN, J. Appl. Phys. 95 (2004) 571–575.

[46] G.V. Bianco, A. Sacchetti, M. Grande, A.D. Orazio, A. Milella, G. Bruno, Effective hole conductivity in nitrogen-doped CVD-graphene by singlet oxygen treatment under photoactivation conditions, Sci. Rep. 12 (2022) 8703.

[47] K. Sekine, Y. Saito, M. Hirayama, T. Ohmi, Highly robust ultrathin silicon nitride films grown at low-temperature by microwave-excitation high-density plasma for giga scale integration, IEEE Trans. Electron Devices 47 (2000) 1370–1374.

[48] K. Awsiuk, A. Psarouli, P. Petrou, A. Budkowski, S. Kakabakos, A. Bernasik, J. Rysz, I. Raptis, Spectroscopic and microscopic examination of protein adsorption and blocking of non-specific binding to silicon surfaces modified with APTES and GOPS, Procedia Eng. 25 (2011) 334–337.

[49] N. Tabet, M. Faiz, A. Al-Oteibi, XPS study of nitrogen-implanted ZnO thin films obtained by DC-Magnetron reactive plasma, J. Electron. Spectrosc. Relat. Phenom. 163 (2008) 15–18.

[50] M.E. Gulseren, G. Kurt, T.G. Ulusoy Ghobadi, A. Ghobadi, G. Salkim, M. Ozturk, B. Butun, E. Ozbay, Investigation of angstrom-thick aluminium oxide passivation layers to improve the gate lag performance of GaN HEMTs, Mater. Res. Express 6 (2019).

[51] M. Grodzicki, J.G. Rousset, P. Ciechanowicz, E. Piskorska-Hommel, D. Hommel, XPS studies on the role of arsenic incorporated into GaN, Vacuum 167 (2019) 73–76.

[52] R. Green, Hall effect measurements in materials characterization, White Pap. (2011) 3111.

[53] O. Philips'Gloeilampenfabrieken, A method of measuring specific resistivity and hall effect of discs of arbitrary shape, Philips Res. Rep. 13 (1958) 1–9.

[54] L.J. van der Pauw, A method of measuring the resistivity and hall coefficient on lamellae of arbitrary shape, Philips Tech. Rev. 20 (1958) 220–224.

[55] T. Kamiya, K. Nomura, H. Hosono, Origins of high mobility and low operation voltage of amorphous oxide TFTs: electronic structure, electron transport, defects and doping, J. Disp. Technol. 5 (2009) 273–288.

[56] A. Reed, C. Stone, K. Roh, H.W. Song, X. Wang, M. Liu, D.-K. Ko, K. No, S. Lee, The role of third cation doping on phase stability, carrier transport and carrier suppression in amorphous oxide semiconductors, J. Mater. Chem. C. 8 (2020) 13798–13810.

[57] K. Tang, S.-L. Gu, J.-D. Ye, S.-M. Zhu, R. Zhang, Y.-D. Zheng, Recent progress of the native defects and p-type doping of zinc oxide, Chin. Phys. B 26 (2017) 047702.

[58] R.-Y. Tian, Y.-J. Zhao, The origin of p-type conduction in (P, N) codoped ZnO, J. Appl. Phys. 106 (2009).

[59] G. Zhang, L. Rebohle, F. Ganss, W. Dawidowski, E. Guziewicz, J.-H. Koh, M. Helm, S. Zhou, Y. Liu, S. Prucnal, P-Type ZnO films made by atomic layer deposition and ion implantation, Nanomaterials 14 (2024) 1069.

[60] S. Herodotou, R.E. Treharne, K. Durose, G.J. Tatlock, R.J. Potter, The effects of zr doping on the optical, electrical and microstructural properties of thin ZnO films deposited by atomic layer deposition, Materials 8 (2015) 7230–7240.

[61] P. Perlin, I. Gorczyca, T. Suski, P. Wisniewski, S. Lepkowski, N. Christensen, A. Svane, M. Hansen, S. DenBaars, B. Damilano, Influence of pressure on the optical properties of $In_xGa_{1-x}N$ epilayers and quantum structures, Phys. Rev. B 64 (2001) 115319.

[62] K. O'Donnell, J. Mosselmans, R. Martin, S. Pereira, M. White, Structural analysis of InGaN epilayers, J. Phys. Condens. Matter 13 (2001) 6977.

[63] J. Li, K.-B. Nam, M.L. Nakarmi, J.-Y. Lin, H. Jiang, P. Carrier, S.-H. Wei, Band structure and fundamental optical transitions in wurtzite AlN, Appl. Phys. Lett. 83 (2003) 5163–5165.

[64] L. Dong, S. Yadav, R. Ramprasad, S. Alpay, Band gap tuning in GaN through equibiaxial in-plane strains, Appl. Phys. Lett. 96 (2010).

[65] A. Lukyanov, J.C. Golden, V. Lubchenko, Structural origin of the midgap electronic states and the urbach tail in pnictogen-chalcogenide glasses, J. Phys. Chem. B 122 (2018) 8082–8097.

[66] N. Zhou, M.G. Kim, S. Loser, J. Smith, H. Yoshida, X. Guo, C. Song, H. Jin, Z. Chen, S.M. Yoon, A.J. Freeman, R.P. Chang, A. Facchetti, T.J. Marks, Amorphous oxide alloys as interfacial layers with broadly tunable electronic structures for organic photovoltaic cells, Proc. Natl. Acad. Sci. USA 112 (2015) 7897–7902.

[67] A.S. Kavasoglu, N. Kavasoglu, S. Oktik, Simulation for capacitance correction from nyquist plot of complex impedance–voltage characteristics, SolidState Electron. 52 (2008) 990–996.

[68] S.K. Saha, A. Guchhait, A.J. Pal, Hybrid pn-junction solar cells based on layers of inorganic nanocrystals and organic semiconductors: optimization of layer thickness by considering the width of the depletion region, Phys. Chem. Chem. Phys. 16 (2014) 4193–4201.